ACS APPLIED MATERIALS & INTERFACES

www.acsami.org

Research Article

Metal–Organic Framework-Based Microfluidic Impedance Sensor Platform for Ultrasensitive Detection of Perfluorooctanesulfonate

Yu H. Cheng,[#] Dushyant Barpaga,[#] Jennifer A. Soltis, V. Shutthanandan, Roli Kargupta, Kee Sung Han, B. Peter McGrail, Radha Kishan Motkuri,[*] Sagnik Basuray,[*] and Sayandev Chatterjee[*]

Cite This: https://dx.doi.org/10.1021/acsami.9b22445

Read Online

ACCESS | Metrics & More | Article Recommendations | Supporting Information

ABSTRACT: The growing global concerns to public health from human exposure to perfluorooctanesulfonate (PFOS) require rapid, sensitive, *in situ* detection where current, state-of-the-art techniques are yet to adequately meet sensitivity standards of the real world. This work presents, for the first time, a synergistic approach for the targeted affinity-based capture of PFOS using a porous sorbent probe that enhances detection sensitivity by embedding it on a microfluidic platform. This novel sorbent-containing platform functions as an electrochemical sensor to directly measure PFOS concentration through a proportional change in electrical current (increase in impedance). The extremely high surface area and pore volume of mesoporous metal–organic framework (MOF) Cr-MIL-101 is used as the probe for targeted PFOS capture based on the affinity of the chromium center toward both the fluorine tail groups as well as the sulfonate functionalities as demonstrated by spectroscopic (NMR and XPS) and microscopic (TEM) studies. Answering the need for an ultrasensitive PFOS detection technique, we are embedding the MOF capture probes inside a microfluidic channel, sandwiched between interdigitated microelectrodes (IDμE). The nanoporous geometry, along with interdigitated microelectrodes, increases the signal-to-noise ratio tremendously. Further, the ability of the capture probes to interact with the PFOS at the molecular level and effectively transduce that response electrochemically has allowed us achieve a significant increase in sensitivity. The PFOS detection limit of 0.5 ng/L is unprecedented for *in situ* analytical PFOS sensors and comparable to quantification limits achieved using state-of-the-art *ex situ* techniques.

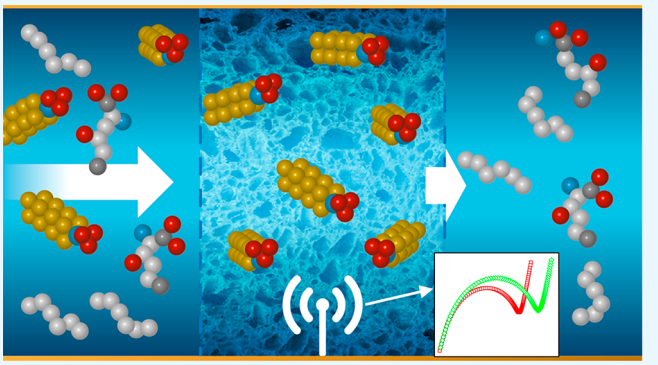

KEYWORDS: *metal–organic frameworks, microfluidics, impedance, perfluorooctanesulfonate, sensing, detection*

INTRODUCTION

The rising global awareness of public vulnerability to chemical, biological, and environmental contamination due to natural or anthropogenic causes as well as deliberate chem–bio threats has heightened the need for sensing techniques that simultaneously offer high sensitivity and selectivity.[1] Developing such methodologies for rapid, ultrasensitive, and highly selective *in situ* detection and quantification of contaminant targets can provide transformative fundamental and technological opportunities across chemical/biological/radiological/nuclear/environmental (CBRNE) forensics and safeguards spaces as well as early detection and diagnostics of diseases and point-of-care applications. This has motivated researchers to focus attention to affinity-based analytical sensors where contaminant detection involves two necessary steps: (i) first, a recognition step that preferentially and selectively captures the target from a sample matrix using specific affinity-based interactions; (ii) second, a transduction step that converts this targeted binding event into a unique, measurable response (namely, electrochemical, spectroscopic, or magnetic).[2] Electrochemical sensors have shown promise in rapid and inexpensive *in situ* target detection. Their working strategy relies on the targeted capture of analytes by uniquely tailored receptor probes immobilized on an electrode platform. In these devices, analyte concentration is directly measured through a proportional change in electrochemical responses (electric current or impedance),[3] which may be converted to electroluminescence[4] or photoluminescence[5] to allow higher sensitivity.

However, the applicability of electrochemical affinity sensors in environmental sensing has been limited by two main concerns. One key challenge of electrochemical sensors is the inability to adequately address low-detection limit concerns that would make them practically relevant as first response

Received: December 11, 2019
Accepted: February 7, 2020
Published: February 7, 2020

Scheme 1. Schematics of PFOS Detection

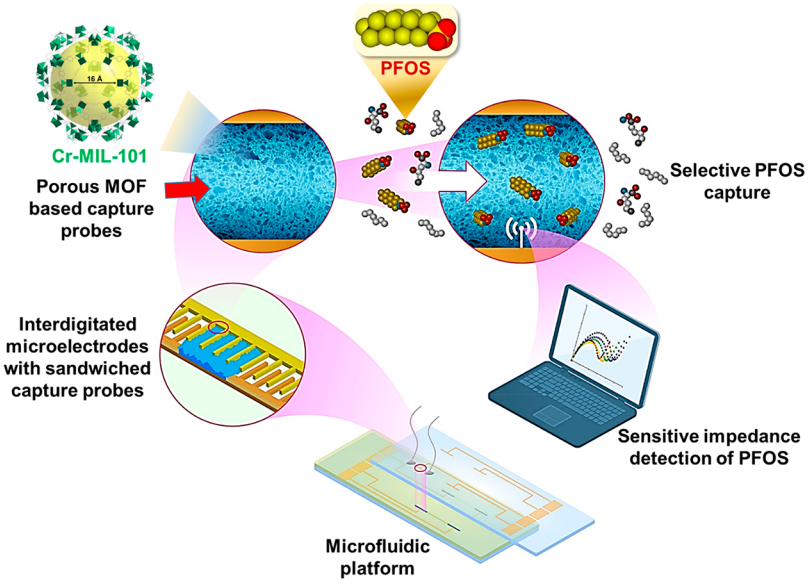

devices. Another key challenge is related to issues in the transduction step that slows down the detection process. The capture mechanism often depends on the diffusion of the target molecule to the recognition element, which translates to long detection times (hours).[6,7] The transducer signal is often complicated by parasitic signals, like double-layer capacitors in electrochemical measurements (false negatives).[8] Thus, the transducer requires bulky and expensive instrumentation to measure changes in the signal due to any binding events.[9,10] In this work, we propose a sensor with a synergistic approach based on a novel combination of receptor design and microfluidic device fabrication to achieve unprecedented sensitivity benefits, as well as rapid detection.

For a proof-of-concept demonstration, we chose as our target analyte of detection an environmental contaminant that is gradually becoming a target of growing concern in the ground and surface water matrices, namely, perfluorooctanesulfonate (PFOS). PFOS is one of the most dominant environmental contributors to the class anthropogenic chemicals commonly known as per- and polyfluoroalkyl substances (PFAS), a group of chemicals that also includes GenX and related chemicals.[11] Their extensive civilian, military, commercial, and industrial uses across the globe over the last few decades have significantly increased their environmental abundance. Unfortunately, their environmental stability and physiological persistence make PFAS a cumulative threat with recent studies linking human exposure to these chemicals to health issues that include elevated cholesterol, obesity, immune suppression, endocrine disruption, and cancer.[12−14] This has dictated the U.S. EPA to set the health advisory level (HAL) for the most commonly studied PFAS (PFOS and its congener with the carboxylic acid functionality, namely, perfluorooctanoic acid [PFOA]) in drinking water to as low as 70 ng/L (either individually or cumulatively). In fact, some of the states in the United States have significantly lower MCLs (as a representative example, in the state of Vermont, the HAL for PFOS is 10 ng/L). Therefore, one of the key practical challenges encountered by *in situ* PFAS analytical sensors is the *inadequate sensitivity* due to ultralow concentrations of the species in the obtained sample.[15−20] To date, existing *in situ* techniques that have been proposed for their detection are unable to meet the desired sensitivity requirements of multicomponent real-world matrices, and therefore, the dominant methods of their analysis require *ex situ* laboratory methods.[11] These methods include analytical scale extraction and subsequent analysis by liquid chromatography tandem mass spectrometry (LC−MS/MS), total oxidizable precursor analysis (TOP),[21] or total fluorine analysis by particle-induced γ-ray emission (PIGE) spectroscopy.[22] However, results obtained from these techniques are either not adaptable for field-deployment or their portable configurations lack the sensitivity requirements. Therefore, a clear need for a highly sensitive *in situ* sensor that is inexpensive and field-deployable exists.

A few instances of affinity-based electrochemical detection of PFAS have been reported;[23,24] although, the proposed designs lacked the sensitivities to adequately detect trace quantities of PFASs. The lack of desired sensitivity arises due to a lack of electrode/probe/target interaction at the molecular level, thereby leading to inefficient sensing as well as transduction.

Our approach proposes to address these drawbacks through improved probe design and improved platform design with unprecedented sensitivities. In this regard, for the first time, we demonstrate an alternative, more sensitive approach using nanoporous metal−organic frameworks (MOFs) as receptor probes to give (i) high sensitivity due to their ultrahigh surface areas and (ii) effective transduction by using them directly on the electrodes as electrode extensions. MOF-based porous materials have achieved maturity in design and technical know-how such that they can be tailored for highly sensitive and selective capture of specific targets; this ability has been applied for their wide use in affinity-based detection of a variety of targets including CO_2, water, ammonia, alcohols, and recently fluorocarbons.[25−33] Further, it has been shown that the enormous surface areas and reactive metal centers of these MOFs allow highly sensitive detection of trace quantities of target analytes. As an example, CO_2 was detected selectively in an oxygen atmosphere using impedance spectroscopy.[34] Recent studies have even demonstrated their high affinity toward fluorine-containing smaller chain fluorocarbons and

https://dx.doi.org/10.1021/acsami.9b22445
ACS Appl. Mater. Interfaces XXXX, XXX, XXX−XXX

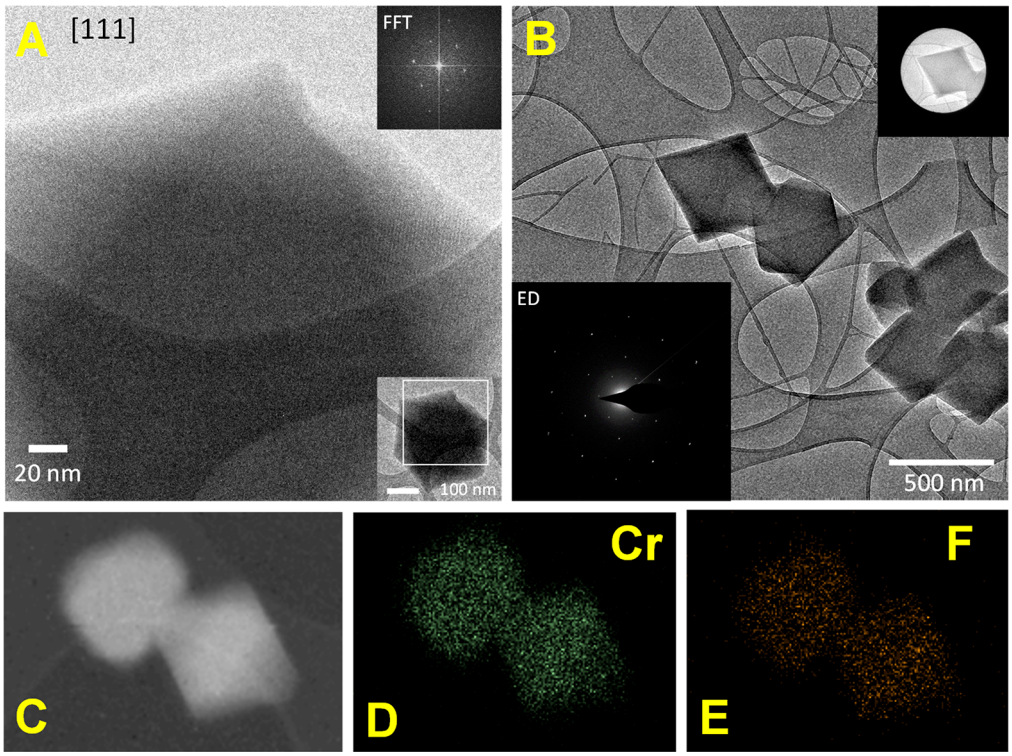

Figure 1. Transmission electron micrographs of Cr-MIL-101. (A) Before and (B) after PFOS exposure. Top right inset of Figure 1A represents a Fast Fourier transform image, while bottom right inset shows a zoomed-out image of a Cr-MIL-101 crystal before PFOS exposure. Top right inset of Figure 1B shows a magnified image of Cr-MIL-101 crystal post-PFOS exposure, while the bottom left inset shows the electron diffraction map. (C) Magnified image of the PFOS-exposed crystals, overlay of the elemental map: (D) Cr distribution on the PFOS-exposed crystals and (E) F distribution on the PFOS-exposed crystals.

also PFAS.[35−41] However, such MOFs were yet to be used in the direct electrochemical sensing of PFAS contaminants. Moreover, their direct use on a microfluidic lab-on-a-chip sensing platform can offer improved transduction to lower the accessible detection limits and offer unprecedented opportunities for the detection of environmental contaminants.[42] Therefore, in this work, we combine a MOF-based receptor with PFOS affinity with nanoporous ultrasensitive capacitive electrode within a microfluidic flow-through platform[43,44] to develop an electrochemical PFOS sensor with high sensitivity, as shown in Scheme 1.

The MOF chosen in this work consists of a hierarchical porous MIL-101 structure based on a Cr metal center that contains two types of mesoporous cages (~25−29 Å) connected through microporous pentagonal (~11.7 Å) and hexagonal windows (~16 Å) for the sensitive capture of PFOS.[45,46] Our choice of Cr-MIL-101 is dictated by two considerations: (i) that the structural integrity of the Cr-MIL-101 is preserved upon PFOS exposure and (ii) the receptor shows high electronic affinity toward PFOS. The integration of these receptors into this platform provides three significant benefits over current PFOS sensors. First, the electrochemical response is facilitated by the nanoporous geometry, with the high signal-to-noise ratio of interdigitated microelectrodes tremendously increasing sensitivity. Nanoconfinement effects further boost the signal. Second, the nanoporous geometry increases convective transport of the target to the biorecognition element, reducing diffusion times, and making the platform more rapid. Third, the convective transport enhancement from the flow removes the parasitic double-layer capacitance signal, allowing rapid measurements of the binding signal at significantly reduced noise. It is notable to mention that although interdigitated electrodes of planar and non-planar geometries have been used before for detection of other, non-PFAS targets (as summarized in Table S1), to the best of our knowledge, herein we present the first example of using a non-planar interdigitated electrode assembly and microfluidic platform for the detection of PFAS.

RESULTS AND DISCUSSION

The key considerations for our choice of receptors for PFOS uptake were dictated by (i) affinity of our receptor toward PFOS and (ii) its stability upon PFOS exposure. For interrogation of stability and affinity, the parent Cr-MIL-101 was compared to the material post-PFOS exposure using microscopic and spectroscopic techniques for an insight into the specific host (Cr-MIL-101) and guest (PFOS) interactions.

To characterize any morphological changes in Cr-MIL-101 upon PFOS exposure as well as to evaluate the microscopic disposition of PFOS onto the Cr-MIL-101 framework, transmission electron microscopy (TEM) was conducted on the MOF samples prior to and post-PFOS exposure. The diffraction patterns of the materials prior to PFOS exposure can be indexed in the $Fd\bar{3}m$ space group and are similar to that reported by Lebedev et al.[47] The electron micrographs shown in Figure 1A indicate well-defined crystals of Cr-MIL-101 whose shape, geometry, and morphology remain nearly unaltered upon PFOS exposure (Figure 1B). The dimensions of the crystals in the unaltered Cr-MIL-101 samples also remain unchanged, and the cubic symmetry of the crystals, as reflected in the shape of the crystals, is also preserved after PFOS exposure, indicating the robust nature of these materials.

https://dx.doi.org/10.1021/acsami.9b22445
ACS Appl. Mater. Interfaces XXXX, XXX, XXX−XXX

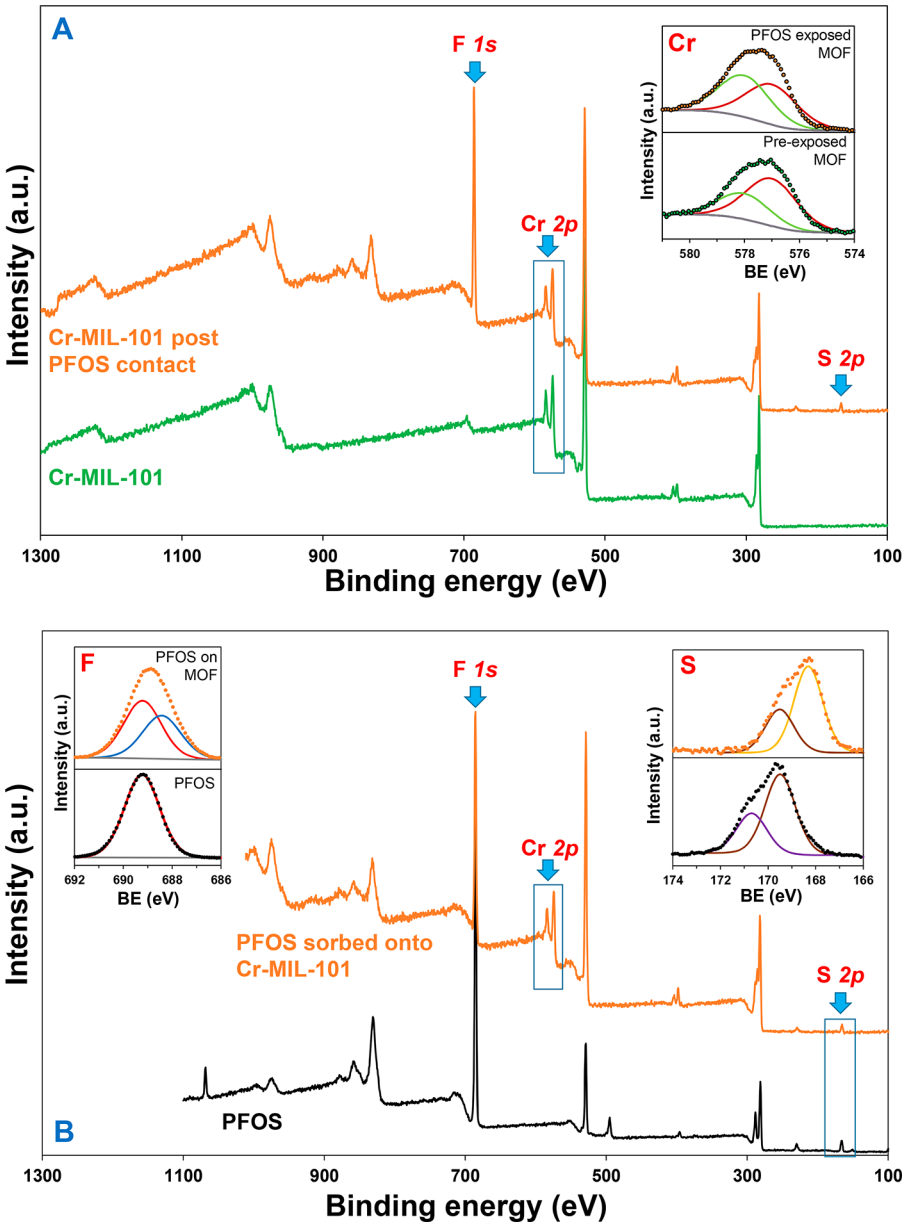

Figure 2. X-ray photoelectron spectra. (A) Cr-MIL-101, (green trace) pre- and (orange trace) postexposure to PFOS; (inset) Cr $3p_{3/2}$ region of Cr-MIL-101, pre- and post-PFOS exposure. (B) (black trace) As-received PFOS and (orange trace) PFOS sorbed onto Cr-MIL-101; (inset left) F 1s region of pristine PFOS and postimmobilization of Cr-MIL-101; (right) S 3p region of pristine PFOS and postimmobilization of Cr-MIL-101. (symbols in the insets) Experimental spectra and (solid lines in the insets) spectral fits.

Elemental mapping shows that postexposure, the F distribution on the crystals nearly shadows the Cr elemental map, indicating an affinity of PFOS for the Cr-MIL-101 material (Figure 1C–E).

The structural integrity of the bulk samples post-PFOS exposure was further characterized using powder X-ray diffraction (PXRD) measurements, as shown in Figure S1. The PXRD pattern of the Cr-MIL-101 sample post-PFOS exposure showed no peak changes/shifts compared to the parent material prior to exposure, clearly indicating no structural alteration of the framework upon adsorption. To directly confirm the presence of PFOS on the MOFs, a ^{19}F solid-state NMR spectrum was also collected on the PFOS-exposed Cr-MIL-101 sample, as shown in Figure S2. Even after flushing the powder sample with DI water to remove any bulk phase concentrations, a clear ^{19}F signal that was not present in the Cr-MIL-101 sample prior to exposure could be observed. The resemblance of this solid-state ^{19}F-NMR spectrum of PFOS-exposed Cr-MIL-101 with the solution ^{19}F-NMR spectrum of PFOS in DI water validates its capture by Cr-MIL-101.

Having confirmed the sorption of PFOS, it was in our interest to probe the host–guest interaction between the MOF metal center and the PFOS to gain further insight into receptor affinity. X-ray photoelectron spectroscopy was conducted on the Cr-MIL-101 materials pre- and post-PFOS exposure to interrogate changes in electron density of the key elements involved in the capture process that can throw light on element-specific affinities (Figure 2). As seen in Figure 2, the full photoelectron profile of the as-received Cr-MIL-101 materials post-PFOS exposure shows clear evidence of capture of PFOS from the appearance of F and S bands in the exposed

https://dx.doi.org/10.1021/acsami.9b22445
ACS Appl. Mater. Interfaces XXXX, XXX, XXX–XXX

material. A closer inspection of the data and comparison with the spectrum of pure Cr-MIL-101, as well as pure PFOS, allows us to arrive at some key conclusions. First, the Cr region of the photoelectron spectrum of the as-received Cr-MIL-101 sample (inset of Figure 2A) showed two Cr environments, as demonstrated by the Cr $2p_{3/2}$ region being resolved into two species with binding energy values of 577.1 and 578.2 eV, respectively, with the lower oxidation state being the dominant contributor (ratio = 4:3). Exposure to PFOS resulted in the higher oxidation state gaining in intensity at the expense of the lower oxidation state (ratio = 1:2), suggesting polarization interaction resulting in oxidation of the Cr center upon contact with PFOS. Specifically, as Cr-MIL-101 is present in large excess compared to the PFOS, it is significant to observe any discernible shift at all in the binding energies of the Cr metal center of the host framework and indicates a strong, favorable sorbent−sorbate interaction. The F region of the spectrum showed a consistent opposite shift; compared to the spectrum of the as-received PFOS, which showed a single 1s line at 689.3 eV, the spectrum of PFOS sorbed onto Cr-MIL-101 showed an additional second F environment with lower binding energy of 688.5 eV; suggesting it gaining in electron density (left inset of Figure 2B). This is suggestive of a synergistic redox process with the F atoms pulling electrons away from the soft Cr center and thereby getting reduced. This is supported by our computational molecular simulation studies between Cr-MIL-101 and a fluorocarbon, the computed radial distribution functions (RDFs) between partially positively charged framework Cr atoms and partially negative charged F of a fluorocarbon, indicating a strong favorable binding Cr···F interaction. Interestingly, the S region of the photoelectron spectrum also showed a shift in the same direction as the F spectrum, albeit with significantly larger magnitude. The S $2p_{3/2}$ line shifted from 169.5 eV in pure PFOS sample to 168.3 eV when PFOS was sorbed onto Cr-MIL-101, suggesting a reduced S oxidation environment in the sorbed sample compared to pure PFOS (right inset of Figure 2B). The large magnitude of this shift indicates a strong affinity between the Cr and the S and may be an indication of the strength of interaction between the MOF framework and the polar, sulfonate head of the PFOS molecule. Our results suggest that although the non-polar CF_3 groups that make up the tail of sorbate have a clear interaction with the framework, it is, in fact, the sulfonate moiety that has a stronger affinity for Cr-MIL-101; a combination of these two can lead to high-PFOS affinity for Cr-MIL-101.

While these experimental observations do throw critical insights into the affinity of the Cr-MIL-101 toward PFOS in deionized water *via* interaction with both the sulfonate head groups and fluorine tails, a key consideration that has the ability to impact and influence the practical application of the sensor is its ability to recognize and capture PFOS from real-world source water matrices. Due to the intricate complexities of multiple components in groundwater systems that make them inherently more complex than river or tap water and a bigger challenge to remediate, it was of our interest to test the ability of the Cr-MIL-101 species to recognize and capture PFOS from groundwater systems. For these preliminary experiments, groundwater collected from the well 299-W19-36 at the Hanford site in Washington, USA, whose composition is listed in Table S2, was utilized, to which PFOS was added at the same concentration as deionized water samples. The ability of the MOF to capture PFOS from this groundwater solution was monitored using ^{19}F NMR, where the resonance intensity of a groundwater sample spiked with 5 mL of 10 mM of PFOS was monitored pre- and postcontact with 5 mg of Cr-MIL-101 for 144 h, as shown in Figure 3.

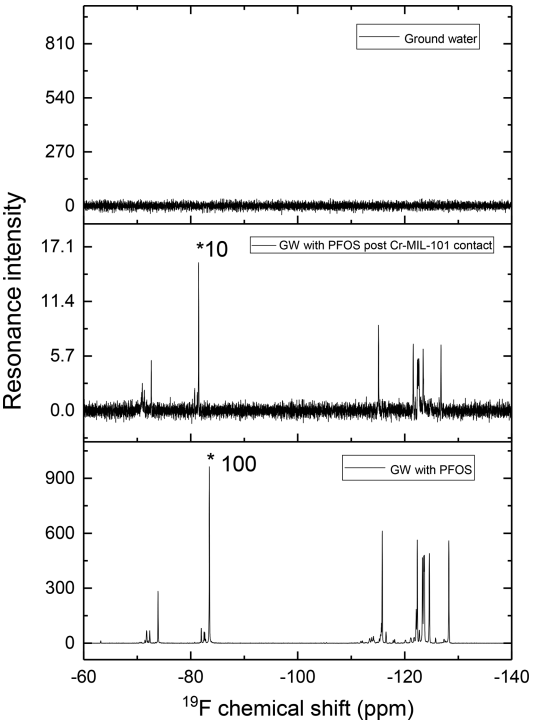

Figure 3. Solution phase ^{19}F NMR spectra. (bottom panel) Spectrum of 5 mL of 10 mM PFOS in groundwater from the well 299-W19-36 at the Hanford site in Washington, USA. (middle panel) Spectrum of the PFOS spiked groundwater collected postcontact with 5 mg of Cr-MIL-101 for 144 h. (top panel) Control spectrum of the groundwater sample without PFOS.

While the initial groundwater sample did not contain any fluorine species, spiking it with PFOS resulted in a distinct PFOS signal. Contact of this PFOS spiked groundwater with Cr-MIL-101 sorbent resulted in a 95% decrease in the intensity of all the fluorine resonances in the solution phase, suggesting the capture of PFOS by the sorbent. This demonstrates the ability of the Cr-MIL-101 to recognize and capture PFOS even in the presence of groundwater cocontaminants. This demonstrates the practical applicability of this probe in more realistic matrices and has implications in the real-world *in situ* sensing of PFOS in groundwater matrices.

It should be noted that the absolute PFOS capacity and uptake rate are yet other performance metrics that will significantly enhance sensitivity measurements from the perspective of receptor probe optimization. Given the highly modular nature of MOF materials, it is possible to use the insights regarding adsorption mechanisms to design and screen potential alternate candidates. However, such experiments are outside the scope of this work and will be explored in detail in subsequent studies; instead, the focus of this work is to utilize a representative high surface area MOF framework in conjunction with a novel sensor device to probe its adsorption affinity for PFOS and enhance detection limits. For this purpose, Cr-MIL-101 has shown remarkable applicability and provided essential design criteria to consider regarding PFOS affinity.

https://dx.doi.org/10.1021/acsami.9b22445
ACS Appl. Mater. Interfaces XXXX, XXX, XXX−XXX

Our insight into the PFOS adsorption affinity of Cr-MIL-101 motivated examination of the direct sensing ability of the MOF toward PFOS recognition and capture. A microfluidic platform consisting of microelectrodes was used to detect the binding of the PFOS to Cr-MIL-101 using electrochemical impedance spectroscopy (EIS). Figure 4 demonstrates the

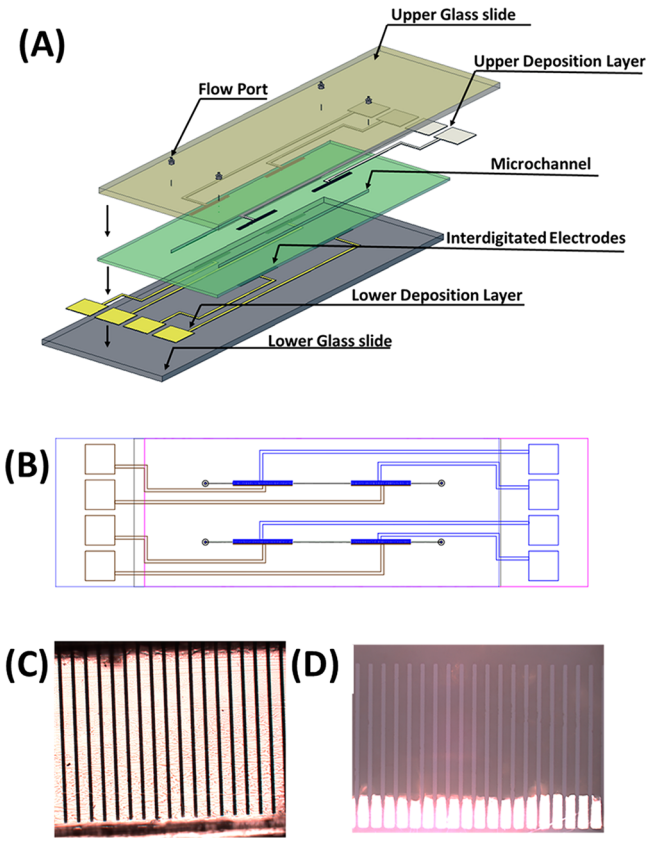

Figure 4. (A) Schematics picture of the non-planar interdigitated device. It shows the microchannel cut from tape, filled with Cr-MIL-101, and sandwiched between the top and bottom interdigitated microelectrode arrays. The placement of the fluid ports is also shown. (B) Top view of the assembled chip. (C) Optical microscopic image of an empty microfluidic channel with interdigitated electrodes. (D) Optical microscopic image of microfluidic channel with interdigitated electrodes filled with Cr-MIL-101.

platform assembly consisting of three layers, top and bottom layers of interdigitated microelectrode array (IDμE) and a middle layer consisting of tightly packed Cr-MIL-101, all contained within a microfluidic channel (the detailed procedure of platform assembly is shown in Figure S4 and elsewhere).[43,44] An array of IDμEs (width 10 μm and length 500 μm) were used to enhance the signal-to-noise ratio compared to that of macro electrodes; while the reduced electrode size/area here restricts mass transport toward its surface and reduces the signal intensity, an accelerated decrease in power drop and background currents lowers the signal-to-noise ratio at a faster rate, significantly improving the net signal.[48,49] Thus, an array of IDμEs has a higher signal-to-noise ratio than a single electrode of the same size. IDμEs as electrochemical transducers offer the added advantages of high collection efficiencies, a low response time that favors rapid detection, low ohmic drop, easy fabrication over multiple substrates, readiness for miniaturization, and eliminates the need for a reference electrode, allowing easy integration with microfluidic chips for multiplexed analytical platforms.

Unlike conventional planar interdigitated IDμE, in this work, we have used a non-planar IDμE (NP-IDμE) to serve multiple purposes (Figure 4). First the NP-IDμE ensures electric field penetration throughout the microfluidic channel width and height. This is critical for a low conductivity receptor such as Cr-MIL-101, unlike conductive materials conventionally used in conjunction with IDμE to increase device sensitivity (examples being carbon nanotubes (CNT) and graphene).[50,51] Consequently the electric field penetration from IDμE into Cr-MIL-101 is minimal and close to the surface. Since the EIS technique detects PFOS binding to Cr-MIL-101 based on changes in the charge transport (and hence the electric current), this limited electric field penetration from planar IDμE would restrict the ability of Cr-MIL-101 to observe minute changes in charge transport and consequently minute changes in target concentrations. The non-planar IDμE chosen in this work ensures the penetration of the electric field across the whole Cr-MIL-101. A set of control experiments were performed, as shown in Figure S9, to test the penetration of the electric field across the entire Cr-MIL-101 layer. In the first experiment shown, we used the chip in the absence of any MOFs in the microfluidic channel and allowed the 0.1X PBS to flow through. In the absence of electron/ion carriers between the electrodes, the response is noisy with very high resistance. The Nyquist response is shown in Figure S9, which indicates an open-circuit response in EIS, implying no charge carriers are exchanged between the electrodes. In a second experiment, we used a copper wire across the top and bottom interdigitated electrode arrays to show the electrical conductivity. The Nyquist response shown in Figure S9 shows up as an inductor in series with a resistor. This is the response of an EIS device that is shorted, thereby indicating that the electrical conductivity of the electrodes on each slide. Finally, in a third setup, when we have a device where the channel is packed with Cr-MIL-101, and the responses are recorded in 0.1 M KCl; the Nyquist behavior (Figure S9) shows a response that is intermediate between an open-circuit response and a short-circuit response. This demonstrates that the circuit path is from the top electrode to the bottom electrode through the Cr-MIL-101 and hence the electric field has penetration throughout the microfluidic channel.

This uniform penetration of the electric field through the Cr-MIL-101 layer allows us to significantly enhance the sensitivity of the nanoporous Cr-MIL-101 electrode extension by being able to capture any change in interfacial charge transport at any position within it, while also preserving the benefits of the Cr-MIL-101 for target capture.

This work also employed a flow-based approach for detection, as opposed to the conventional stationary methods. In our approach, microelectrodes, along with the receptor probes, were aligned in the microfluidic channel; detection involved the equilibration of the channel and the receptor probes with a blank buffer solution, which was followed by flowing the sample solution through the channel, resulting in target capture. This flow-based approach helps to overcome the diffusion-based solution resistance and allows for faster measurement and data collection. Further, the nanoporosity along with the flow ensures maximal binding of the PFOS with the Cr-MIL-101 due to decreased diffusion from the increased convective transport.

https://dx.doi.org/10.1021/acsami.9b22445
ACS Appl. Mater. Interfaces XXXX, XXX, XXX−XXX

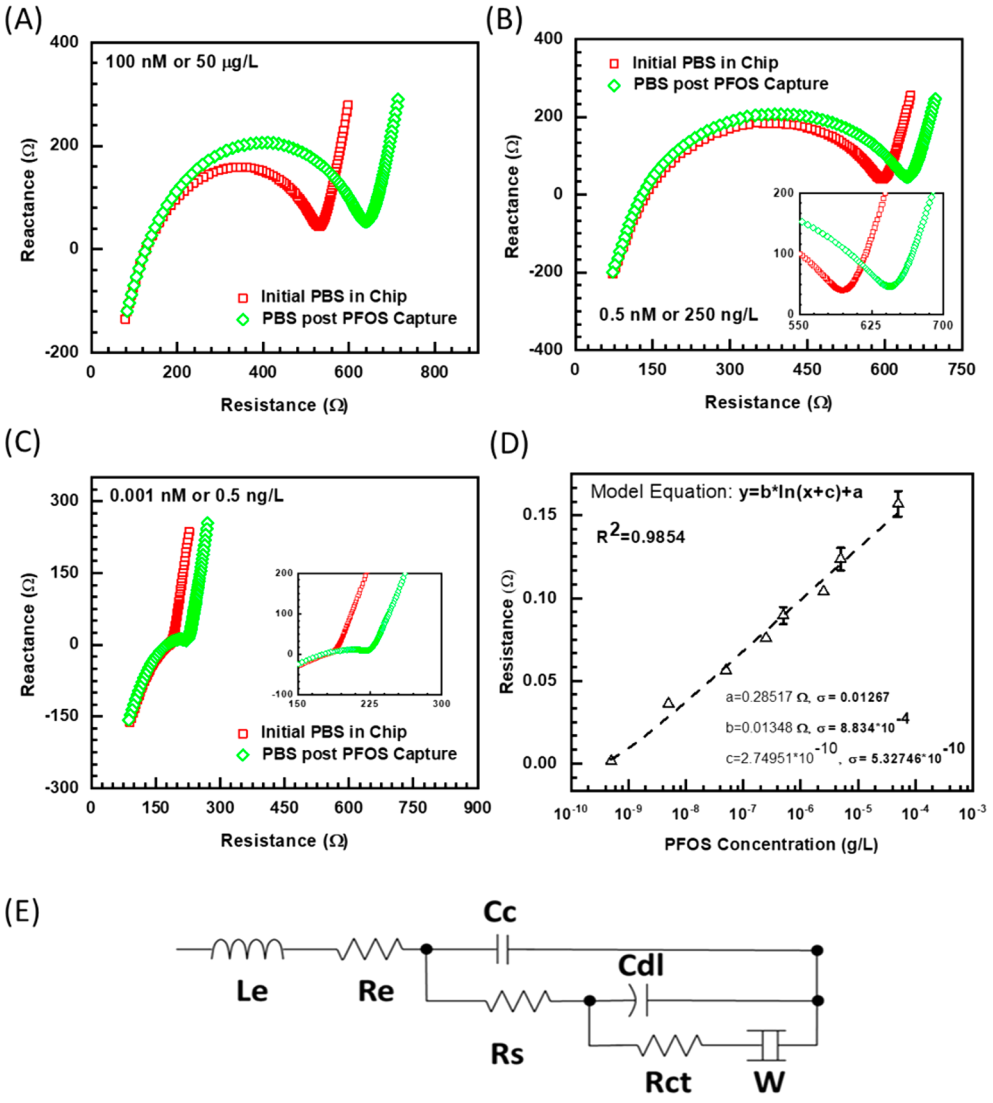

Figure 5. Nyquist plot of the EIS response of the Cr-MIL-101 in 0.1X PBS buffer before and postexposure to (A) 50 μg/L PFOS, (B) 250 ng/L PFOS, and (C) 0.05 ng/L PFOS. (D) Calibration curve of the normalized increase in the charge transfer resistance (Rct) from Cr-MIL-101 with increasing PFOS concentrations in 0.1X PBS, indicating progressively increased PFOS binding. The error bars are obtained from standard deviations based on three independent measurements for each of the concentrations. The Rct values are obtained by fitting the Nyquist plot to the equivalent circuit in (E) using Zview software.

It is well established in EIS that at low frequencies (Hz) the current is dominated by the charge transfer resistance (electron transfer between electrode surface and electrolyte), while at high frequencies (kHz to MHz) the double-layer capacitor (interfacial polarization of the electrolyte) dominates. Typically the electrode surface or the charge transfer resistance is of interest to most people working with EIS-based sensors as it is an accurate representation of the signal from the sensor (typically an electrode). The double-layer capacitor is seen as a parasitic signal and the most significant source of noise in EIS. Hence, EIS is generally recorded at lower frequencies to overcome the parasitic double-layer capacitance (Cdl). However, low-frequency EIS is plagued by low signal-to-noise and environmental disturbances. Thus, it becomes significantly more challenging to measure low-frequency EIS and detect subsequent changes in the EIS spectrum.

Further, the time needed to measure EIS at a low frequency increases from instantaneous at high-frequency EIS to a couple of minutes at low-frequency EIS. To address this, we employed a tight packing of the Cr-MIL-101 receptors within the microfluidic channel; such close packing resulted in disruption of the double-layer capacitor due to the higher Péclet number (convective fluxes) from the nanoporous packing density akin to a packed bed reactor. This shifts the relaxation frequency of the double-layer capacitor to high frequency (MHz), allowing us to observe the charge transfer or polarization resistance at much higher frequencies (kHz). This allowed us to measure EIS at significantly higher frequency ranges (until 1 kHz) with an applied AC voltage of 100 mV, allowing us twin advantages over conventional EIS measurement, namely, rapid measurements and enhanced signal-to-noise.

The EIS spectrum (Nyquist curve) of Cr-MIL-101 in 0.1 M PBS buffer was characterized by a conventional semicircular region followed by a linear region. The introduction of PFOS in the analyte stream of PBS buffer showed a marked change in the impedance profile of the Cr-MIL-101 receptors compared to that of the buffer solution itself, with a discernible increase in the radius of curvature of the semicircular region of the

https://dx.doi.org/10.1021/acsami.9b22445
ACS Appl. Mater. Interfaces XXXX, XXX, XXX−XXX

Nyquist curves shown in Figure 5. The EIS response upon PFOS capture by Cr-MIL-101 receptors packed between the NP-IDμE was modeled using the transmission line equivalent circuit model (commonly used for porous IDμE) shown in Figure 5 using Zview software.[52,53] In the equivalent circuit, Re is the inherent resistance in the device, Le is the parasitic inductor in the device due to external noises, Rs is the resistance of the solution filling the device, Cdl is the double-layer capacitance, Rct is the charge transfer resistance, Ws is the Warburg element as the impedance associated with the diffusion rate of the reactants, and Cc is the direct capacitance between the two electrodes (Figure 4). Cc or the cell capacitance is the capacitance between the two non-planar finger electrode combs of the NP-IDμE. Rs, the resistance of the solution, represents the total impedance of the interface between the gold electrode and electrolyte. Cdl is the double-layer capacitance that is due to the interfacial ionic polarization between the electrolyte and the tightly packed Cr-MIL-101 receptors. Rct and the Warburg impedance are in series and are parallel to Cdl since both phenomena occur simultaneously. The charge transfer or polarization resistance Rct is associated with the transfer of the electrons from the electrolyte onto the tightly packed Cr-MIL-101 receptors. Rct is heavily dependent on several factors like the available surface area of the tightly packed Cr-MIL-101 receptors among others. Hence, the capture and binding of PFOS by Cr-MIL-101 presumably leads to alteration of the charge transfer or polarization resistance due to change in the available electrode surface area. This is the key contributor to the sensor signal, with all other circuit elements being chiefly parasitic and not contributing significantly. On the basis of this model, the increase in the radius of curvature of the semicircular region indicates that the charge transfer resistance (Rct) increases in the Cr-MIL-101 post-PFOS exposure (Figure 5; the detailed plots are shown in Figure S5; the fits are shown in Figures S6 and S7).

To quantify the effect of varying PFOS concentrations as well as to account for the non-identical MOF loading from across chips, the EIS signal from the chip was normalized using the relation 1:

$$\text{Symbol} = \left(\frac{R_{\text{PFOS}} - R_{\text{MOF}}}{R_{\text{MOF}}} \right) \quad (1)$$

where R_{PFOS} and R_{MOF} are the charge transfer resistance (Rct) from Cr-MIL-101 post-PFOS exposure and prior to PFOS exposure, respectively. Using this normalization scheme, the charge transfer resistance showed a linear correlation with PFOS concentrations (Figure 5), allowing us to establish a limit of quantification based on the smallest concentration of PFOS that we were able to accurately analyze using this setup. Based on this, a limit of quantification of 0.5 ng/L is obtained which, to our knowledge, is unprecedented for portable approaches for PFOS detection and quantification.

Our achieved quantification limits thus far are significantly lower than other electrochemical methodologies reported thus far; notably, potentiometric methods using fluorous membrane ion-selective electrodes achieved a detection limit of ~0.07 ppb or 70 ng/L,[23] while a more recent report using MIP method achieved a detection limit of 0.04 nM (20 ng/L) for PFOS.[54] Using similar MIP-based receptor probes albeit a different, complementary detection technique such (namely, photo-electrochemical mode) showed electrode dependent variations, namely, using hybrid AgI-BiOI hybrid microelectrodes, the limit of PFOA detection was indirectly estimated as 10 ng/L (i.e., 0.01 ppb).[55] On the contrary, TiO_2-based micro-electrodes resulted in a significant decline in the sensitivities, with the LOD being estimated as 86000 ng/L (or 86 ppb).[4] However, our method shows a significant improvement as we can directly detect, measure, and quantify a concentration of 0.5 ng/L (i.e., 0.5 ppt) rather than relying on an indirect estimation, indicating a superior sensitivity of our approach. Further, based on our previous observations that a luminescent mode can further enhance sensitivities, our method can be improved to achieve further lower LODs.

The obtained limit of quantification is significantly improved compared to other techniques and methodologies, namely, HPLC−FLD and GC−ECD[56] techniques (around 10 ppb to 1 ppm) and colorimetry (10 ppb). Therefore, our method shows an unprecedented limit of quantification compared to other prevalent *in situ* techniques and is comparable to state-of-the-art *ex situ* techniques. (Comparison of different methods for sensing and quantification of PFAS are listed in Table 1, Section S5). Currently, the most accepted approach to PFOA/PFOS analysis is LC−MS/MS methods, which could allow for better detection limits (0.01 ppt−0.01 ppb).[57] However, the reported lowest detection limits with LC−MS/MS require pre-treatment and pre-concentration steps, and therefore, may not be readily adapted for portable deployments, demonstrating the value of our methodology for rapid, on-site PFOS detection.

Table 1. Comparison the Limits of Detection (LOD) for PFOS with Our Portable Electrochemical Technique Relative to Various State-of-the Art Lab-Based *Ex Situ* Techniques

technique	LOD	reference
LC−MS/MS: liquid chromatography tandem mass spectrometry	~1 ng/L	Chen et al.[23]
TOF MS: time-of-flight mass spectrometry	1−10 ng/L	Berger et al.[63]
PIGE: fluorine by particle-induced γ-ray emission spectroscopy	~10 nmol/cm^2	Schaider et al.[22]
NMR: nuclear magnetic resonance	10 μg/L	Weiss-Errico et al.[64]
TOP: total oxidizable precursor	1−10 ng/L	Zhang et al.[65]
Our electrochemical technique	0.5 ng/L	This work

CONCLUSIONS

Overall, this work demonstrates a microfluidic, affinity-based electrochemical sensor platform for rapid PFOS detection that offers unprecedented sensitivity through a combination of receptor probe design, electrode configuration, and their combination within the microfluidic lab-on-a-chip platform. Our approach of using MOF-based receptor probes for targeted PFOS capture offers high specific affinity benefits, while the non-planar interdigitated microelectrode design ensures the potential limitations to sensitivity that could arise from using the non-conductive Cr-MIL-101-based MOF receptors as electrode extensions are eliminated. The non-planar electrodes ensure the penetration of the electric field across the whole Cr-MIL-101, which enables the use of these receptors directly on a sensing platform, thereby allowing us to capture even the minutest of changes in interfacial charge transport at any position within it. This leads to a high

https://dx.doi.org/10.1021/acsami.9b22445
ACS Appl. Mater. Interfaces XXXX, XXX, XXX−XXX

sensitivity of 0.5 ng/L, as opposed to 70 ng/L set by the United States Environmental Protection Agency, which is unprecedented for *in situ* analytical PFOS sensors. Further, the close packing of the receptors within the microfluidic channel due to the nanoporosity allows us to operate at high frequencies, which allows for rapid detection and analysis.

The ability of Cr-MIL-101 to recognize PFOS from a multicomponet groundwater matrix and demonstrate near quantitative capture represents significant implications of this work for environmental monitoring. The added benefit of the proposed methodology is that this work can be readily expanded to other targets as well. While most of the present regulations are focused on PFOS, or its carboxylate analogue perfluorooctanoic acid (PFOA), there are a total of ∼6500 different PFAS molecules that are known, with recent studies showing that the smaller chains can be more toxic (namely, GenX). This work provides a proof-of-concept of the detection of PFOS and its quantification at levels significantly lower than the health advisory limits. It also provides a strategy by which similar techniques can be designed for the detection and quantification of other PFAS targets (such as GenX) through the design of the capture probe. Furthermore, this design can also be extended to other challenging contaminants of interest through design and selection of appropriate receptor probes and can also be synergized with alternate approaches of contaminant capture, recognition, and detection, opening promising new opportunities in the diverse areas of CBRNE detection.[58,59]

EXPERIMENTAL SECTION

Chemicals and Materials. Chromium(III) nitrate nonahydrate ($Cr(NO_3)_3{\cdot}9H_2O$) and terephthalic acid (BDC) were obtained from Sigma-Aldrich and were used as received. Perfluorooctanesulfonic acid (PFOS; 40% in water) was obtained from Sigma-Aldrich. *N*, *N*-dimethylformamide was obtained from Alfa Aesar and was used without further purification. Ultrapure water (resistivity ≥18 MΩ) was used during the experimental process. Standard glass slides (1304G) with ground edges, 90° corners, and size 25 mm × 75 mm × 1 mm were used for impedance measurements and were procured from Globe Scientific Inc., Mahwah, New Jersey, USA. Double-sided polypropylene (PP) tape (90880) with SR-26 silicone pressure-sensitive adhesives on both sides and a thickness of 142 μm was obtained from ARcare. Adhesives Research Inc., Glen Rock, Pennsylvania, USA. A PBS buffer (1X) was obtained from VWR.

For testing the recognition of PFOS from groundwater matrices, the groundwater medium was collected from the well 299-W19-36 at the Hanford site in Washington, U.S. The major inorganic constituents present in the groundwater are listed in Table S2.[60,61]

Instrumentations. For electrochemical experiments, the fabrication of the microelectrode assembly was done at the Nanofabrication Facility Advanced Science Research Centre at the City University of New York. A 4294A precision impedance analyzer from Keysight Technologies was used for all the electrochemical impedance measurements. A EVG620 mask aligner from EV Group was used for contact lithography. A NE-300 syringe pump obtained from New Era Pump Systems, Inc, Farmingdale, New York, USA. was used for solution injection.

The characterization of the materials upon PFOS capture was done using correlative microscopic, spectroscopic, and diffraction measurements consisting of solid-state ^{19}F nuclear magnetic resonance (NMR), infrared (IR) and X-ray photoelectron (XPS) spectroscopies, transmission electron microscopes (TEM), and powder X-ray diffraction (PXRD) studies. Liquid-state ^{19}F NMR measurements were performed on a 750 MHz NMR spectrometer (Agilent, Santa Clara, California, USA) with a 5 mm wideband HXY probe at room temperature as a function of time with the time interval of 30 min up to ∼40 h. ^{19}F NMR spectra were accumulated on the Larmor frequency of 705.83 MHz using a single pulse excitation. Solid-state ^{19}F NMR spectra were accumulated with a 4 mm HFXY magic angle spinning (MAS) probe on a 600 MHz solid-state NMR spectrometer (Agilent) on the Larmor frequency of 564.68 MHz using a spin−echo sequence at spinning speed of 14 kHz. The ^{19}F chemical shift for both liquid- and solid-state experiments was calibrated with CF_3CH_2OH (−78 ppm) as an external reference.

X-ray photoelectron spectroscopy (XPS) analysis was performed using a Kratos Axis Ultra DLD spectrometer, which consists of an Al Kα monochromatic X-ray source (1486.6 eV) and a high-resolution spherical mirror analyzer. The X-ray source was operated at 105 W, and the emitted photoelectrons were collected at the analyzer entrance slit normal to the sample surface. The data acquisition was carried out in hybrid mode with analysis area of 700 μm × 300 μm. The survey spectra were collected at pass energy of 160 eV with a 0.5 eV step size, and high-resolution spectra were recorded at pass energy of 40 eV with step size of 0.1 eV. The pass energy 40 eV in the 700 μm × 300 μm analysis area is referred to the fwhm of 0.7 eV for Ag $3d_{5/2}$. The charge neutralizer with low energy electrons was used to compensate the surface charge buildup at the surface. All the XPS peaks were charge referenced to C 1s binding energy at 285 eV. XPS data were analyzed by CasaXPS software using mixed Gaussian/Lorentzian (GL(30)) line shape and Shirley background correction.

PXRD was used to analyze the structural integrity of the materials. Experiments were performed with a Rigaku MiniFlex 600 X-ray diffractometer (XRD). The sample was placed in a powder sample holder under ambient conditions, and a pattern was collected from the 2θ range 1−50°. The step size was 2° min^{-1}.

TEM data were collected using two instruments. The sample not exposed to PFOS was imaged on an FEI Titan 80-300 Environmental TEM equipped with a field emission electron gun and operated at 300 kV under low-dose conditions. Images were collected with a US 1000 2k × 2k charge capture device (CCD) camera (Gatan, Inc.) operated *via* Digital Micrograph (Gatan, Inc.). The PFOS-exposed sample was imaged in an FEI Tecnai T20 TEM (Thermo Fisher Scientific) equipped with a field emission gun and operating at 200 keV in bright field and scanning TEM modes. Image capture was performed on an FEI Eagle charge capture device (CCD) camera using TIA software (Thermo Fisher Scientific). Energy-dispersive X-ray spectroscopy (EDS) was performed using an EDAX TEAM EDS Analysis System equipped with a silicon drift detector (EDAX Inc.).

Specimens for TEM were prepared by sonicating the suspended solids in ethanol for 3 min before placing a single drop on a 200-mesh copper TEM grid coated with holey carbon film (Electron Microscopy Supplies) and allowing it to dry. The drop was pipetted from the upper portion of the supernatant to maximize the likelihood of capturing particles that were thin enough for TEM and electron diffraction, rather than those large enough to settle due to gravity.

Receptor Probe. *Cr-MIL-101.* Cr-MIL-101 was synthesized under hydrothermal conditions following the literature protocols,[62] as described in the Supporting Information Section S1.

Cr-MIL-101 Exposed to PFOS. MOF samples were exposed to a 10 mM aqueous PFOS solution with subsequent DI water washes to leave behind only adsorbed phase concentrations.

Chip Fabrication and PFOS Sensing Protocol. The procedure for the microfluidic chip fabrications described in the Supporting Information Section S2, and the similar scheme is shown in Figure S3. The subsequent packing of the Cr-MIL-101 is described in Section S3, while the sensing protocol is described in Section S4. The readers are directed to other publications by the Basuray group to get more insight into the device.[43,44] Three independent EIS measurements were recorded at each experimental concentrations to ensure reproducibility and reliability of measurements.

ASSOCIATED CONTENT

Supporting Information

The Supporting Information is available free of charge at https://pubs.acs.org/doi/10.1021/acsami.9b22445.

https://dx.doi.org/10.1021/acsami.9b22445
ACS Appl. Mater. Interfaces XXXX, XXX, XXX−XXX

Discussions of receptor probe synthesis and characterization, chip fabrications, microchannel design and packing, PFOS sensing protocol, and limit of detection comparison, figures of PXRD spectra, ^{19}F NMR spectra, schematics for fabrication protocol, protocol for platform assembly, experimental EIS overlays, and Nyquist curves, and tables of comparisons of electrode system sensitivity and groundwater composition (PDF)

AUTHOR INFORMATION

Corresponding Authors

Radha Kishan Motkuri − *Energy and Environment Directorate, Pacific Northwest National Laboratory, Richland, Washington 99352, United States;* orcid.org/0000-0002-2079-4798; Email: Radhakishan.Motkuri@pnnl.gov

Sagnik Basuray − *Department of Chemical and Materials Engineering, New Jersey Institute of Technology, Newark, New Jersey 07102, United States*; Email: sagnik.basuray@njit.edu

Sayandev Chatterjee − *Energy and Environment Directorate, Pacific Northwest National Laboratory, Richland, Washington 99352, United States;* orcid.org/0000-0003-2218-5635; Email: Sayandev.Chatterjee@pnnl.gov

Authors

Yu H. Cheng − *Department of Chemical and Materials Engineering, New Jersey Institute of Technology, Newark, New Jersey 07102, United States*

Dushyant Barpaga − *Energy and Environment Directorate, Pacific Northwest National Laboratory, Richland, Washington 99352, United States;* orcid.org/0000-0003-2271-6213

Jennifer A. Soltis − *National Security Directorate, Pacific Northwest National Laboratory, Richland, Washington 99352, United States*

V. Shutthanandan − *Environmental and Molecular Sciences Laboratory, Pacific Northwest National Laboratory, Richland, Washington 99352, United States;* orcid.org/0000-0003-2957-7535

Roli Kargupta − *Department of Chemical and Materials Engineering, New Jersey Institute of Technology, Newark, New Jersey 07102, United States*

Kee Sung Han − *Physical and Computational Sciences Directorate, Pacific Northwest National Laboratory, Richland, Washington 99352, United States;* orcid.org/0000-0002-3535-1818

B. Peter McGrail − *Energy and Environment Directorate, Pacific Northwest National Laboratory, Richland, Washington 99352, United States*

Complete contact information is available at: https://pubs.acs.org/10.1021/acsami.9b22445

Author Contributions

#Y.H.C. and D.B. contributed equally to this work.

Notes

The authors declare no competing financial interest.

ACKNOWLEDGMENTS

This research was supported by (1) the Laboratory Directed Research and Development Program at the Pacific Northwest National Laboratory (SEED EED) (S.C. and R.K.M.) and (2) a National Science Foundation (NSF) Career grant (#1751759) to S.B. We also acknowledge the U.S. Department of Energy's (DOE) Geothermal Technologies Office (GTO) for MOF materials development. The Pacific Northwest National Laboratory (PNNL) is operated by Battelle for the U.S. Department of Energy under Contract DE-AC05-76RL01830. Part of this research was performed at the Environmental Molecular Sciences Laboratory, a national scientific user facility at PNNL managed by the Department of Energy's Office of Biological and Environmental Research.

REFERENCES

(1) Chen, L.; McBranch, D. W.; Wang, H. L.; Helgeson, R.; Wudl, F.; Whitten, D. G. Highly Sensitive Biological and Chemical Sensors Based on Reversible Fluorescence Quenching in a Conjugated Polymer. *Proc. Natl. Acad. Sci. U. S. A.* **1999**, *96* (22), 12287−12292.

(2) Chatterjee, S.; Fujimoto, M. S.; Cheng, Y. H.; Kargupta, R.; Soltis, J. A.; Kishan Motkuri, R.; Basuray, S. Improving the Sensitivity of Electrochemical Sensors through a Complementary Luminescent Mode: A New Spectroelectrochemical Approach. *Sens. Actuators, B* **2019**, *284*, 663−674.

(3) Daniels, J. S.; Pourmand, N. Label-free Impedance Biosensors: Opportunities and Challenges. *Electroanalysis* **2007**, *19* (12), 1239−1257.

(4) Tran, T. T.; Li, J. Z.; Feng, H.; Cai, J.; Yuan, L. J.; Wang, N. Y.; Cai, Q. Y. Molecularly Imprinted Polymer Modified TiO2 Nanotube Arrays for Photoelectrochemical determination of perfluorooctane sulfonate (PFOS). *Sens. Actuators, B* **2014**, *190*, 745−751.

(5) Chatterjee, S.; Del Negro, A. S.; Edwards, M. K.; Bryan, S. A.; Kaval, N.; Pantelic, N.; Morris, L. K.; Heineman, W. R.; Seliskar, C. J. Luminescence-Based Spectroelectrochemical Sensor for [Tc(dmpe)-3]2+/+ (dmpe = 1,2-bis(dimethylphosphino)ethane) within a Charge-Selective Polymer Film. *Anal. Chem.* **2011**, *83* (5), 1766−1772.

(6) Baronas, R. Nonlinear Effects of Diffusion Limitations on the Response and Sensitivity of Amperometric Biosensors. *Electrochim. Acta* **2017**, *240*, 399−407.

(7) Baronas, R.; Kulys, J.; Lancinskas, A.; Zilinskas, A. Effect of Diffusion Limitations on Multianalyte Determination from Biased Biosensor Response. *Sensors* **2014**, *14* (3), 4634−4656.

(8) Stern, E.; Wagner, R.; Sigworth, F. J.; Breaker, R.; Fahmy, T. M.; Reed, M. A. Importance of the Debye Screening Length on Nanowire Field Effect Transistor Sensors. *Nano Lett.* **2007**, *7* (11), 3405−3409.

(9) Han, K. N.; Li, C. A.; Seong, G. H. Microfluidic Chips for Immunoassays. *Annu. Rev. Anal. Chem.* **2013**, *6* (1), 119−141.

(10) Mohammed, M. I.; Desmulliez, M. P. Lab-on-a-chip Based Immunosensor Principles and Technologies for the Detection of Cardiac Biomarkers: A Review. *Lab Chip* **2011**, *11* (4), 569−595.

(11) Barzen-Hanson, K. A.; Roberts, S. C.; Choyke, S.; Oetjen, K.; McAlees, A.; Riddell, N.; McCrindle, R.; Ferguson, P. L.; Higgins, C. P.; Field, J. A. Discovery of 40 Classes of Per- and Polyfluoroalkyl Substances in Historical Aqueous Film-Forming Foams (AFFFs) and AFFF-Impacted Groundwater. *Environ. Sci. Technol.* **2017**, *51* (4), 2047−2057.

(12) Grandjean, P.; Andersen, E. W.; Budtz-Jorgensen, E.; Nielsen, F.; Molbak, K.; Weihe, P.; Heilmann, C. Serum Vaccine Antibody Concentrations in Children Exposed to Perfluorinated Compounds. *Jama-J. Am. Med. Assoc* **2012**, *307* (4), 391−397.

(13) Braun, J. M.; Chen, A. M.; Romano, M. E.; Calafat, A. M.; Webster, G. M.; Yolton, K.; Lanphear, B. P. Prenatal Perfluoroalkyl Substance Exposure and Child Adiposity at 8 Years of Age: The HOME Study. *Obesity* **2016**, *24* (1), 231−237.

(14) Barry, V.; Winquist, A.; Steenland, K. Perfluorooctanoic Acid (PFOA) Exposures and Incident Cancers among Adults Living Near a Chemical Plant. *Environ. Health Perspect.* **2013**, *121* (11−12), 1313−1318.

(15) Luz, R. A. S.; Iost, R. M.; Crespilho, F. N. Nanomaterials for Biosensors and Implantable Biodevices. In *Nanobioelectrochemistry: From Implantable Biosensors to Green Power Generation*; Crespilho, F. N., Ed.; Springer Berlin Heidelberg: Berlin, Germany, 2013; pp 27−48.

(16) Ricci, F.; Adornetto, G.; Palleschi, G. A Review of Experimental Aspects of Electrochemical Immunosensors. *Electrochim. Acta* **2012**, *84*, 74−83.
(17) Baldrich, E.; Munoz, F. X. Carbon Nanotube Wiring: A Tool for Straightforward Electrochemical Biosensing at Magnetic Particles. *Anal. Chem.* **2011**, *83* (24), 9244−9250.
(18) Lisdat, F.; Schafer, D. The Use of Electrochemical Impedance Spectroscopy for Biosensing. *Anal. Bioanal. Chem.* **2008**, *391* (5), 1555−1567.
(19) Fan, X.; White, I. M.; Shopova, S. I.; Zhu, H.; Suter, J. D.; Sun, Y. Sensitive Optical Biosensors for Unlabeled Targets: A Review. *Anal. Chim. Acta* **2008**, *620* (1−2), 8−26.
(20) Wang, J. Carbon-Nanotube Based Electrochemical Biosensors: A Review. *Electroanalysis* **2005**, *17* (1), 7−14.
(21) Houtz, E. F.; Sedlak, D. L. Oxidative Conversion as a Means of Detecting Precursors to Perfluoroalkyl Acids in Urban Runoff. *Environ. Sci. Technol.* **2012**, *46* (17), 9342−9349.
(22) Schaider, L. A.; Balan, S. A.; Blum, A.; Andrews, D. Q.; Strynar, M. J.; Dickinson, M. E.; Lunderberg, D. M.; Lang, J. R.; Peaslee, G. F. Fluorinated Compounds in US Fast Food Packaging. *Environ. Sci. Technol. Lett.* **2017**, *4* (3), 105−111.
(23) Chen, L. D.; Lai, C. Z.; Granda, L. P.; Fierke, M. A.; Mandal, D.; Stein, A.; Gladysz, J. A.; Buhlmann, P. Fluorous Membrane Ion-Selective Electrodes for Perfluorinated Surfactants: Trace-Level Detection and in Situ Monitoring of Adsorption. *Anal. Chem.* **2013**, *85* (15), 7471−7477.
(24) Chen, S. H.; Li, A. M.; Zhang, L. Z.; Gong, J. M. Molecularly Imprinted Ultrathin Graphitic Carbon Nitride Nanosheets-Based Electrochemiluminescence Sensing Probe for Sensitive Detection of Perfluorooctanoic acid. *Anal. Chim. Acta* **2015**, *896*, 68−77.
(25) Liu, R. L.; Liu, Y. R.; Yu, S. H.; Yang, C. L.; Li, Z. F.; Li, G. A Highly Proton-Conductive 3D Ionic Cadmium-Organic Framework for Ammonia and Amines Impedance Sensing. *ACS Appl. Mater. Interfaces* **2019**, *11* (1), 1713−1722.
(26) Motkuri, R. K.; Thallapally, P. K.; Annapureddy, H. V. R.; Dang, L. X.; Krishna, R.; Nune, S. K.; Fernandez, C. A.; Liu, J.; McGrail, B. P. Separation of Polar Compounds Using a Flexible Metal-Organic Framework. *Chem. Commun.* **2015**, *51* (40), 8421−8424.
(27) Lee, J. S.; Vlaisavljevich, B.; Britt, D. K.; Brown, C. M.; Haranczyk, M.; Neaton, J. B.; Smit, B.; Long, J. R.; Queen, W. L. Understanding Small-Molecule Interactions in Metal-Organic Frameworks: Coupling Experiment with Theory. *Adv. Mater.* **2015**, *27* (38), 5785−5796.
(28) Das, A. K.; Vemuri, R. S.; Kutnyakov, I.; McGrail, B. P.; Motkuri, R. K. An Efficient Synthesis Strategy for Metal-Organic Frameworks: Dry-Gel Synthesis of MOF-74 Framework with High Yield and Improved Performance. *Sci. Rep.* **2016**, *6*, DOI: 10.1038/srep28050.
(29) Zheng, J.; Barpaga, D.; Gutierrez, O. Y.; Browning, N. D.; Mehdi, B. L.; Farha, O. K.; Lercher, J. A. M. B. P.; Motkuri, R. K. Exceptional Fluorocarbon Uptake with Mesoporous Metal-Organic Frameworks for Adsorption-Based Cooling Systems. *ACS Applied Energy Materials* **2018**, *1* (11), 5853−5858.
(30) Hanikel, N.; Prevot, M. S.; Fathieh, F.; Kapustin, E. A.; Lyu, H.; Wang, H. Z.; Diercks, N. J.; Glover, T. G.; Yaghi, O. M. Rapid Cycling and Exceptional Yield in a Metal-Organic Framework Water Harvester. *ACS Cent. Sci.* **2019**, *5* (10), 1699−1706.
(31) Motkuri, R. K.; Annapureddy, H. V. R.; Vijaykumar, M.; Schaef, H. T.; Martin, P. F.; McGrail, B. P.; Dang, L. X.; Krishna, R.; Thallapally, P. K. Fluorocarbon Adsorption in Hierarchical Porous Frameworks. *Nat. Commun.* **2014**, *5*, .
(32) Chen, Z. J.; Li, P. H.; Zhang, X.; Li, P.; Wasson, M. C.; Islamoglu, T.; Stoddart, J. F.; Farha, O. K. Reticular Access to Highly Porous acs-MOFs with Rigid Trigonal Prismatic Linkers for Water Sorption. *J. Am. Chem. Soc.* **2019**, *141* (7), 2900−2905.
(33) Liu, J.; Zheng, J.; Barpaga, D.; Sabale, S.; Arey, B.; Derewinski, M. A.; McGrail, B. P.; Motkuri, R. K. A Tunable Bimetallic MOF-74 for Adsorption Chiller Applications. *Eur. J. Inorg. Chem.* **2018**, *2018* (7), 885−889.
(34) Gassensmith, J. J.; Kim, J. Y.; Holcroft, J. M.; Farha, O. K.; Stoddart, J. F.; Hupp, J. T.; Jeong, N. C. A Metal-Organic Framework-Based Material for Electrochemical Sensing of Carbon Dioxide. *J. Am. Chem. Soc.* **2014**, *136* (23), 8277−8282.
(35) Liu, K.; Zhang, S. Y.; Hu, X. Y.; Zhang, K. Y.; Roy, A.; Yu, G. Understanding the Adsorption of PFOA on MIL-101(Cr)-Based Anionic-Exchange Metal-Organic Frameworks: Comparing DFT Calculations with Aqueous Sorption Experiments. *Environ. Sci. Technol.* **2015**, *49* (14), 8657−8665.
(36) Zheng, J.; Vemuri, R. S.; Estevez, L.; Koech, P. K.; Vargas, T.; Camaioni, D. M.; Blake, T. A.; McGrail, B. P.; Motkuri, R. K. Pore-Engineered Metal-Organic Frameworks with Excellent Adsorption of Water and Fluorocarbon Refrigerant for Cooling Applications. *J. Am. Chem. Soc.* **2017**, *139* (31), 10601−10604.
(37) Chen, M. J.; Yang, A. C.; Wang, N. H.; Chiu, H. C.; Li, Y. L.; Kang, D. Y.; Lo, S. L. Influence of Crystal Topology and Interior Surface Functionality of Metal-Organic Frameworks on PFOA Sorption Performance. *Microporous Mesoporous Mater.* **2016**, *236*, 202−210.
(38) Zheng, J.; Barpaga, D.; Trump, B.; Shetty, M.; Fan, Y.; Bhattacharya, P.; Jenks, J.; Su, C.-Y.; Brown, C.; Maurin, G.; McGrail, B. P.; Motkuri, R. K. Molecular Insight into Fluorocarbon Adsorption in Expanded Metal-Organic Framework Analogs. *J. Am. Chem. Soc.* **2020**, *142*, 3002−3012.
(39) Sini, K.; Bourgeois, D.; Idouhar, M.; Carboni, M.; Meyer, D. Metal-Organic Framework Sorbents for the Removal of Perfluorinated Compounds in an Aqueous Environment. *New J. Chem.* **2018**, *42* (22), 17889−17894.
(40) Li, Y. X.; Yang, Z. X.; Wang, Y. L.; Bai, Z. L.; Zheng, T.; Dai, X.; Liu, S. T.; Gui, D. X.; Liu, W.; Chen, M.; Chen, L. H.; Diwu, J.; Zhu, L. Y.; Zhou, R. H.; Chai, Z. F.; Albrecht-Schmitt, T. E.; Wang, S. A Mesoporous Cationic Thorium-organic Framework that Rapidly Traps Anionic Persistent Organic Pollutants. *Nat. Commun.* **2017**, *8*, .
(41) Barpaga, D.; Nguyen, V.; Medasani, B. K.; Chatterjee, S.; McGrail, B. P.; Motkuri, R. K.; Dang, L. X. Insight into Fluorocarbon Adsorption in Metal-Organic Frameworks via Experiments and Molecular Simulations. *Sci. Rep.* **2019**, *9*, 10289.
(42) Drummond, T. G.; Hill, M. G.; Barton, J. K. Electrochemical DNA sensors. *Nat. Biotechnol.* **2003**, *21* (10), 1192−1199.
(43) Cheng, Y. H.; Moura, P. A. R.; Zhenglong, L.; Feng, L.; Arokiam, S.; Yang, J.; Hariharan, M.; Basuray, S. Effect of electrode configuration on the sensitivity of nucleic acid detection in a non-planar, flow-through, porous interdigitated electrode. *Biomicrofluidics* **2019**, *13* (6), 064118.
(44) Li, Z.; Cheng, Y.-H.; Feng, L.; Felix, D. D.; Neil, J.; Antonio, R. M. P.; Rahman, M.; Yang, J.; Azizighannad, S.; Mitra, S.; Basuray, S. Communication—Electrochemical Impedance Signature of a Non-Planar, Interdigitated, Flow-Through, Porous, Carbon-Based Microelectrode. *J. Electrochem. Soc.* **2019**, *166* (16), B1669−B1672.
(45) Latroche, M.; Surble, S.; Serre, C.; Mellot-Draznieks, C.; Llewellyn, P. L.; Lee, J. H.; Chang, J. S.; Jhung, S. H.; Ferey, G. Hydrogen storage in the giant-pore metal-organic frameworks MIL-100 and MIL101. *Angew. Chem., Int. Ed.* **2006**, *45* (48), 8227−8231.
(46) Ferey, G.; Mellot-Draznieks, C.; Serre, C.; Millange, F.; Dutour, J.; Surble, S.; Margiolaki, I. A Chromium Terephthalate-based Solid with Unusually Large Pore Volumes and Surface Area. *Science* **2005**, *309* (5743), 2040−2042.
(47) Lebedev, O. I.; Millange, F.; Serre, C.; Van Tendeloo, G.; Ferey, G. First Direct Imaging of Giant Pores of the Metal-Organic Framework MIL-101. *Chem. Mater.* **2005**, *17* (26), 6525−6527.
(48) Wightman, R. M. Detection Technologies. Probing Cellular Chemistry in Biological Systems with Microelectrodes. *Science (Washington, DC, U. S.)* **2006**, *311* (5767), 1570−4.
(49) Cahill, P. S.; Walker, Q. D.; Finnegan, J. M.; Mickelson, G. E.; Travis, E. R.; Wightman, R. M. Microelectrodes for the Measurement

https://dx.doi.org/10.1021/acsami.9b22445
ACS Appl. Mater. Interfaces XXXX, XXX, XXX−XXX

of Catecholamines in Biological systems. *Anal. Chem.* **1996**, *68* (18), 3180−3186.
(50) He, Q.; Wu, S.; Yin, Z.; Zhang, H. Graphene-based Electronic Sensors. *Chemical Science* **2012**, *3* (6), 1764−1772.
(51) Ding, S.; Das, S. R.; Brownlee, B. J.; Parate, K.; Davis, T. M.; Stromberg, L. R.; Chan, E. K. L.; Katz, J.; Iverson, B. D.; Claussen, J. C. CIP2A Immunosensor Comprised of vertically-aligned carbon nanotube interdigitated electrodes towards point-of-care oral cancer screening. *Biosens. Bioelectron.* **2018**, *117*, 68−74.
(52) Kaushik, A.; Yndart, A.; Kumar, S.; Jayant, R. D.; Vashist, A.; Brown, A. N.; Li, C. Z.; Nair, M. A Sensitive Electrochemical Immunosensor for Label-free Detection of Zika-virus Protein. *Sci. Rep.* **2018**, *8* (1), 9700.
(53) Ding, S.; Mosher, C.; Lee, X. Y.; Das, S. R.; Cargill, A. A.; Tang, X.; Chen, B.; McLamore, E. S.; Gomes, C.; Hostetter, J. M.; Claussen, J. C. Rapid and Label-Free Detection of Interferon Gamma via an Electrochemical Aptasensor Comprising a Ternary Surface Monolayer on a Gold Interdigitated Electrode Array. *ACS Sens* **2017**, *2* (2), 210−217.
(54) Karimian, N.; Stortini, A. M.; Moretto, L. M.; Costantino, C.; Bogialli, S.; Ugo, P. Electrochemosensor for Trace Analysis of Perfluorooctanesulfonate in Water Based on a Molecularly Imprinted Poly(o-phenylenediamine) Polymer. *Acs Sensors* **2018**, *3* (7), 1291−1298.
(55) Gong, J. M.; Fang, T.; Peng, D. H.; Li, A. M.; Zhang, L. Z. A Highly Sensitive Photoelectrochemical Detection of Perfluorooctanic acid with Molecularly Imprined Polymer-Functionalized Nano-architectured Hybrid of AgI-BiOI Composite. *Biosens. Bioelectron.* **2015**, *73*, 256−263.
(56) Scott, B. F.; Moody, C. A.; Spencer, C.; Small, J. M.; Muir, D. C. G.; Mabury, S. A. Analysis for Perfluorocarboxylic Acids/Anions in Surface Waters and Precipitation using GC-MS and Analysis of PFOA from Large-volume Samples. *Environ. Sci. Technol.* **2006**, *40* (20), 6405−6410.
(57) de Voogt, P.; Saez, M. Analytical Chemistry of Perfluoroalkylated Substances. *TrAC, Trends Anal. Chem.* **2006**, *25* (4), 326−342.
(58) Chatterjee, S.; Norton, A. E.; Edwards, M. K.; Peterson, J. M.; Taylor, S. D.; Bryan, S. A.; Andersen, A.; Govind, N.; Albrecht-Schmitt, T. E.; Connick, W. B.; Levitskaia, T. G. Highly Selective Colorimetric and Luminescence Response of a Square-Planar Platinum(II) Terpyridyl Complex to Aqueous TcO4(−). *Inorg. Chem.* **2015**, *54* (20), 9914−9923.
(59) Barpaga, D.; Zheng, J.; Han, K. S.; Soltis, J. A.; Shutthanandan, V.; Basuray, S.; McGrail, B. P.; Chatterjee, S.; Motkuri, R. K. Probing the Sorption of Perfluorooctanesulfonate Using Mesoporous Metal-Organic Frameworks from Aqueous Solutions. *Inorg. Chem.* **2019**, *58* (13), 8339−8346.
(60) Levitskaia, T. G.; Chatterjee, S.; Arey, B. W.; Campbell, E. L.; Hong, Y. C.; Kovarik, L.; Peterson, J. M.; Pence, N. K.; Romero, J.; Shutthanandan, V.; Schwenzer, B.; Varga, T. RedOx-controlled Sorption of Iodine Anions by Hydrotalcite Composites. *RSC Adv.* **2016**, *6* (79), 76042−76055.
(61) Mattigod, S. V.; Wellman, D. M.; Golovich, E. C.; Cordova, E.; Smith, R. M. *Adsorption on Selected Activated Carbons*; Pacific Northwest National Laboratory: Richland, WA, 2010.
(62) Guo, Q.; Ren, L. M.; Kumar, P.; Cybulskis, V. J.; Mkhoyan, K. A.; Davis, M. E.; Tsapatsis, M. A Chromium Hydroxide/MIL-101(Cr) MOF Composite Catalyst and Its Use for the Selective Isomerization of Glucose to Fructose. *Angew. Chem., Int. Ed.* **2018**, *57* (18), 4926−4930.
(63) Berger, U.; Haukas, M. Validation of a Screening Method based on Liquid Chromatography Coupled to High-resolution Mass Spectrometry for Analysis of Perfluoroalkylated substances in Biota. *J. Chromatogr A* **2005**, *1081* (2), 210−217.
(64) Weiss-Errico, M. J.; Ghiviriga, I.; O'Shea, K. E. F-19 NMR Characterization of the Encapsulation of Emerging Perfluoroether-carboxylic Acids by Cyclodextrins. *J. Phys. Chem. B* **2017**, *121* (35), 8359−8366.
(65) Zhang, C. H.; Hopkins, Z. R.; McCord, J.; Strynar, M. J.; Knappe, D. R. U. Fate of Per- and Polyfluoroalkyl Ether Acids in the Total Oxidizable Precursor Assay and Implications for the Analysis of Impacted Water. *Environ. Sci. Technol. Lett.* **2019**, *6* (11), 662−668.

https://dx.doi.org/10.1021/acsami.9b22445
ACS Appl. Mater. Interfaces XXXX, XXX, XXX−XXX